

Characterization of a gaseous time projection chamber with an internal ^{37}Ar source*

Wenming Zhang,^{1,†} Yuanchun Liu,^{1,†} Ke Han,^{1,‡} Shaobo Wang,^{1,2,§} Xiaopeng Zhou,³ and Xunan Guo³

¹*INPAC and School of Physics and Astronomy, Shanghai Jiao Tong University,*

MOE Key Lab for Particle Physics, Astrophysics and Cosmology,

Shanghai Key Laboratory for Particle Physics and Cosmology, Shanghai 200240, China

²*SPEIT (SJTU-Paris Elite Institute of Technology), Shanghai Jiao Tong University, Shanghai 200240, China*

³*School of Physics, Beihang University, Beijing 102206, China*

We report on a systematic characterization of a gaseous time projection chamber based on Micromegas using an internal ^{37}Ar source. The ^{37}Ar is a fast-decaying and low-energy calibration source that provides a mono-energetic peak of 2.82 keV. Gaseous ^{37}Ar source is injected and uniformly distributed in argon-(2.5%)isobutane mixtures. Key performance parameters of the detector, such as electron transmission, gain, energy resolution, gain uniformity, and drift field evolution, are effectively and quickly calibrated. The maximum attainable gain is up to thousands at pressures from 0.3 to 10 bar. The gain uniformity, related to the homogeneity of the avalanche gap of Micromegas, is calibrated quickly thanks to the event-by-event position reconstruction and quasi-point energy deposition of ^{37}Ar . The energy resolution is improved with the obtained gain uniformity map. The most noticeable improvement in energy resolution from 44.9% to 35.4% is observed at 7 bar working pressure. The internal calibration source is also used to characterize the dependence of the detector's electric field distortion on the drift field. An electrostatic field simulation confirms our measured dependence.

Keywords: Time projection chambers, Micromegas, ^{37}Ar , Internal calibration

I. INTRODUCTION

Time Projection Chambers (TPCs) have been widely used in nuclear and particle physics experiments since their invention in the 1970s [1]. The gaseous TPCs can record both energy depositions and three-dimensional trajectories of charged particles traveling within. They have applications in the collider experiments (e.g., ALICE [2], STAR [3]), Neutrinoless Double Beta Decay (NLDBD) experiments (e.g., NEXT [4], PandaX-III [5, 6], R2D2 [7], NuDEX [8]), and dark matter direct detections (e.g., TREX-DM [9], NEWS [10]) due to the characteristics of excellent energy resolution and imaging capability.

The calibration of gaseous TPCs is critical for understanding their performance. The calibration directly influences the accuracy, reliability, and interpretability of the results of experiments. Future large-scale detectors require efficient, convenient, and comprehensive calibration methods. Calibrations with radioactive sources [11, 12] and cosmic rays [13, 14] are widely used. Radioactive sources such as ^{55}Fe , ^{241}Am , and ^{232}Th are commonly used as a point source, but the efficiency is restricted for the calibration of gas detectors with a large sensitive area. It is also difficult to mount and remove the source inside the TPC volume after the detector has been commissioned. Cosmic rays with penetrating power and relatively uniform energy deposition per unit length allow

us to characterize key performances of TPCs, such as the drift velocity and electron lifetime [15]. However, the continuous energy spectrum of cosmic rays causes non-negligible errors in calculating the gain and energy resolution.

Fast decaying gaseous sources, such as ^{220}Rn , ^{83m}Kr , and ^{37}Ar , can be directly mixed into the gas medium and provide an alternate method for the calibration of gaseous TPCs. ^{37}Ar decays to stable ^{37}Cl by electron capture with a half-life of 35 days, and the associated K-, L- and M-shell electron binding energies are 2.82 keV, 0.27 keV, and 0.0175 keV, respectively. The first demonstration of a sub-keV electron recoil energy threshold in a dual-phase liquid argon time projection chamber is obtained with the ^{37}Ar source by observing the peaks in the energy spectrum at 2.82 keV and 0.27 keV [16]. The low-energy peaks of ^{37}Ar have been used to extend the low-energy threshold of dual-phase xenon TPCs for dark matter detections [17–20].

We present a comprehensive internal calibration using ^{37}Ar source for a gaseous TPC at different working pressures ranging from 0.3 bar to 10 bar in this paper, which represents the first try to introduce an ^{37}Ar source into a gaseous TPC. The ^{37}Ar source has two advantages over the traditional ^{55}Fe source for gaseous TPC. The unique combination of homogeneous distribution in the TPC volume, quasi-point source energy deposition of low-energy peaks, and gaseous TPC's event-by-event position reconstruction capability makes ^{37}Ar highly efficient in calibrating detector response uniformity and electric field distortion. ^{37}Ar can be easily dissolved into and separated from the detector, which is convenient for real-time periodic calibration of the detector.

The TPC contains an active volume of about 8 L with a 20.0 cm drift distance. The detector can be operated up to 15 bar. The working gas is argon-(2.5%)isobutane gas mixtures in this work. The isobutane used as a quencher in argon gas improves the detector gain and resolution attributed to the Penning effect [21]. To ensure insulation and sup-

* This work is supported by grant No.U1965201 and No.11905127 from the National Natural Sciences Foundation of China and grant 2016YFA0400302 from the Ministry of Science and Technology of China. We thank the support from the Key Laboratory for Particle Physics, Astrophysics and Cosmology, Ministry of Education. We thank the support from the Double First Class Plan of Shanghai Jiao Tong University.

† These authors contributed equally to this work.

‡ Corresponding author, ke.han@sjtu.edu.cn

§ Corresponding author, shaobo.wang@sjtu.edu.cn

port the detector, an electric field shaping cage (field cage, in short) made of an acrylic cylinder with a diameter of 34.0 cm and a height of 20.0 cm is employed. The field cage comprises copper rings, on which voltage divider resistors are carefully arranged to generate a uniform drift electric field in the drift volume. One Micromegas module (Micro-Mesh Gaseous Structure) [22] is used for charge readout in the TPC. The Micromegas is a successful Micro Pattern Gas Detector (MPGD) technique, consisting of a thin metallic grid (commonly called mesh) and an anode plane separated by insulating pillars. Both structures define a small avalanche gap (between 20 and 300 μm), where ionized electrons generated in the drift volume are amplified. This technology is widely used in particle and nuclear physics. It has proven to have many advantages, such as its high granularity, good energy resolution, easy construction, gain stability, and the radiopurity of the materials used to make these charge readouts.

In the internal calibration, the 2.82-keV peak from the ^{37}Ar source is used to calculate the gain and energy resolution of the detector under different pressures. Correspondingly, the electron transmission and gain curves are presented with various amplification fields and drift fields. The gain uniformity of the detector, mainly resulting from the homogeneity of the avalanche gap between the mesh and the anode of Micromegas, is calculated with uniformly distributed ^{37}Ar events and then used to improve the reconstructed charge and subsequently energy resolution of acquired events. The gains we acquired can check Micromegas's gain uniformity map and ensure the detector's stable operation under high gas pressure. We have also quantified the drift field evolution with ^{37}Ar events, which impacts the effective area of the detector. The corresponding results are corroborated with simulations using the COMSOL Multiphysics software [23].

This article first details the experimental setup in Section II. Then, the experimental procedure and data taking are described in Section III. The results and discussion in terms of electron transmission, gain, energy resolution, gain uniformity, and drift field evolution with ^{37}Ar calibration method are shown in Section IV. Finally, we finish in Section V with the conclusions of this work.

II. EXPERIMENTAL SETUP

The experimental setup used is shown in Fig. 1. The core component is a gaseous TPC, which consists of a readout plane with a side length of 19.5 cm on the top, a cathode with a diameter of 34.0 cm at the bottom, and a cylindrical field cage with a height of 20.0 cm in the middle. The active volume of the TPC is approximately 8 L which is defined as the drift volume enclosed by the readout plane, the field cage, and the cathode. The readout plane comprises one Micromegas module mounted on a circular aluminum holding plate, defined as the horizontal XY plane, with the drift field pointing towards the vertical Z direction. The field cage is suspended from the holding plate of the readout plane. It comprises an acrylic barrel that provides a mechanical structure, and ten copper rings serve as electrodes. Ten 1 G Ω re-

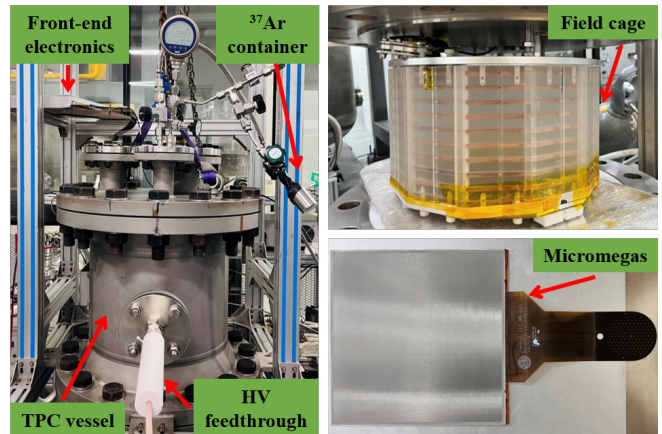


Fig. 1. (Color online) Pictures of the experimental setup, including the TPC pressure vessel (left), the field cage (top-right), and the thermal-bonding Micromegas module (bottom-right).

sistors are placed between adjacent sets of copper rings for degraded electric potentials. The cathode is simply an aluminum mesh connected to the bottom ring of the field cage. The negative high voltage (HV) is applied to the aluminum cathode through a high-pressure feedthrough on one of the ports on the side wall of the TPC pressure vessel. In our TPC, electric field lines point from top to bottom, and ionized electrons drift upward in the field cage.

The Micromegas module is fabricated with the so-called thermal-bonding technology [24, 25], which makes an amplification structure by pressing the stretched stainless steel (SS) mesh directly against insulating pillars on the readout printed circuit board (PCB) anode using a hot rolling machine. The readout PCB is attached to a high-purity, oxygen-free copper substrate to provide a rigid support for resisting the tension of the SS mesh. A germanium (Ge) layer is coated using the thermal evaporation method on the surface of the readout PCB as a resistive anode to suppress the discharge and improve the performance of the detector [26]. The insulating pillars made of the thermal-bonding film are used to support the SS mesh onto the readout PCB anode, creating an avalanche gap of 100 μm . The Micromegas module has an active area of $19.5 \times 19.5 \text{ cm}^2$. It has 64 strips in each direction (X and Y) embedded in the inner layer of the readout PCB anode for signal readout, and the pitch size of the strip is 3 mm. A strip readout scheme is chosen to reduce the number of readout channels in the readout PCB anode and the energy deposition on the Micromegas is shared between X and Y strips. Thermal-bonding technology has the advantages of low-cost, straightforward production procedures and convenient gap size adjustment through pillar replacement while maintaining the excellent performance of the manufactured detectors. However, it is worth noting that the size of the avalanche gap of Micromegas is determined by the thickness of the pillars. Its uniformity over the whole active area is a crucial property, as it directly affects the detector's energy resolution and ensures stable operation under high gas pressure. The surface smoothness of the anode plate of Micromegas

and the conditions such as temperature and pressure in the thermal-bonding process can affect the size of the avalanche gap as well.

The electronics and DAQ (Data Acquisition) system reads out signals from Micromegas strips upon triggering them and subsequently digitizes and writes the data to disk. The strip signals are digitized by the commercial ASAD (front-end board, ASIC Support, and Analog-Digital conversion) and CoBo (back-end board, Concentration Board) solution [27, 28] based on AGET (ASIC for Generic Electronic system for TPCs) chips [28]. The AGET chips are widely used in gaseous TPCs for particle and nuclear physics experiments. They have sampling frequencies of up to 100 MHz, dynamic ranges from 120 fC to 10 pC, and peaking time from 50 ns to 1 μ s. The wide dynamic ranges and adjustable sampling frequencies enable us to flexibly obtain event data with various optional configurations to satisfy different experimental requirements. A Field Programmable Gate Array (FPGA) on the ASAD board controls the AGET chips and sends the packets of collected data to the CoBo card. A CoBo card reads up to four ASAD boards, and an ASAD board hosts four AGET chips, each of which can process 64 strip channels from the detector input. Therefore, in the configuration of this experiment, two AGET chips are activated for the Micromegas module with 128 strip channels, half of which are in the X direction and the other half in the Y direction. The DAQ system we use is shipped with the ASAD/CoBo solution. It reads and writes configuration parameters of ASAD/CoBo, manages the data-taking process, monitors data quality, and periodically presents acquired waveforms. All of our measurements adopt the so-called "multiplicity" trigger mode in the DAQ configuration. The "multiplicity" refers to the number of channels over a threshold generated by the AGET chip comparing channel inputs with a preset trigger threshold.

The gaseous TPC hangs from the top flange of an SS pressure vessel, which can be operated at pressures up to 15 bar. The pressure vessel consists of a cylindrical main body with a thickness of 1.8 cm, in conjunction with top and bottom flanges, both of which are 3.5 cm thick. The inner diameter of the cylindrical main body is about 38.8 cm and the height is 47.0 cm, creating an inner volume of approximately 60 L. Two DN-50 ports are located in the middle of the cylindrical main body for high-voltage feedthrough of the cathode and vacuum pumping. The pump port is connected to a dry fore-pump (PTS300 from Agilent) and a turbo pump (HiPace300 from Pfeiffer), and a vacuum of better than 10^{-5} mbar can be achieved. The flat top and bottom flanges are fastened onto the cylindrical main body by 16 M33 bolts. Three ports on the top and bottom flanges are utilized for Micromegas signals and HV bias, gas inlet and outlet, and as backups, respectively. Micromegas signals from the readout plane are transmitted through the DN-65 port of the top flange via custom-made Kapton extension cable feedthroughs.

The gas system of the TPC is shown in Fig. 2. It is connected to the gas inlet and outlet of the pressure vessel, performing gas filling, circulation, purification, and recovery for the experiment. Due to the outgassing of the detector materials like acrylic, the quality of the gas mixture in the vessel de-

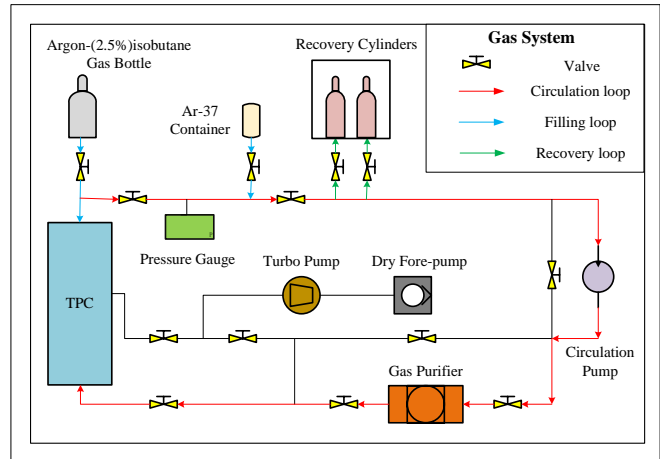


Fig. 2. (Color online) Schematic diagram of the gas system of the TPC.

teriorates over time. To mitigate this, continuous purification with a circulation loop is necessary. A room-temperature gas purifier [29] installed in the gas system can effectively eliminate impurities such as H_2O , O_2 , CO , and CO_2 from gases with the assistance of a magnetically driven circulation pump. Gas recovery can be performed in the line of the gas system with two 500 ml recovery cylinders. When immersed in a liquid nitrogen dewar during operation, the recovery cylinders function as an absorption pump and liquify argon for storage. All the pipes are connected using Swagelok VCR metal gasket face seal fittings, with designed working pressures of up to 15 bar.

A small ^{37}Ar SS container (0.1 bar pressure, 25 ml volume, as shown in Fig. 1) and a pre-mixed argon-(2.5%)isobutane gas bottle (40 L volume, 40 bar pressure) are connected onto the gas system for gas filling. The isotope ^{37}Ar is produced by irradiation of 99.9%-enriched ^{36}Ar gas with thermal neutrons: $^{36}Ar(n, \gamma)^{37}Ar$. The enriched ^{36}Ar contained in a quartz glass ampule is used for irradiation with a capture cross-section of about 5 b. The enrichment enhances the production of ^{37}Ar and reduces the production of undesired isotopes. After irradiation, the activated gas is cryogenically extracted from the quartz glass ampule, transferred to a small SS container, and pressurized to 0.1 bar. An initial ^{37}Ar activity of about 100 Bq per SS container is expected according to the neutron flux, the neutron capture cross-section of ^{36}Ar , and the irradiation time.

III. EXPERIMENTAL PROCEDURE AND DATA TAKING

The TPC pressure vessel is pumped below 1×10^{-5} mbar before injecting the activated ^{37}Ar gas from the 25 ml SS container. Subsequently, pre-mixed argon-(2.5%)isobutane gas mixtures are injected into the vessel to 1 bar as a starting point. Two recovery cylinders in a liquid nitrogen dewar are connected to the vessel to reduce pressure to 0.3 bar by liquifying argon, thereby exploring the detector's low-

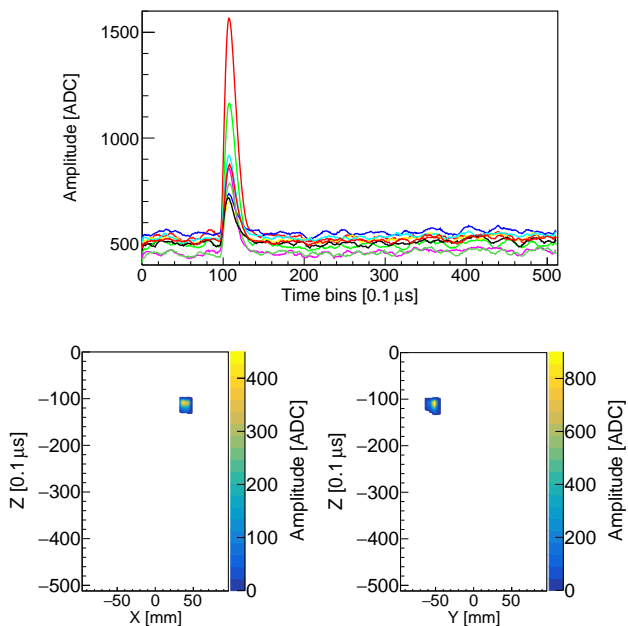


Fig. 3. (Color online) (top) Waveforms of an ^{37}Ar K-shell decay event. (bottom) Images of an ^{37}Ar K-shell decay event on the XZ and YZ planes.

pressure performance. After the low-pressure measurement is completed, 1 bar of argon gas in the vessel is recovered from two recovery cylinders, and then the gas pressure is increased up to 10 bar by injecting the pre-mixed argon gas mixtures for high-pressure measurements.

The ^{37}Ar gas source is used to characterize the detector performance. The X-ray and Auger electrons from the source decay deposit energy by ionizing the gas atoms in the TPC drift volume, and the ionized electrons drift along the electric field to the readout plane. Finally, the ionized electrons are amplified in the avalanche gap and then collected by the Micromegas strips in X and Y directions. The strip signals are digitized by the ASAD-CoBo electronics with a record length of 512 sampling points and a sampling frequency of 10 MHz (resulting in a time window of $51.2\ \mu\text{s}$). The horizontal position of an event is determined by the triggered strips in the XY readout plane. Moreover, the timing information of strip signals provides a relative position measurement in the vertical Z direction. Therefore, a complete three-dimensional image of an event is recorded.

An example of ^{37}Ar K-shell decay events, including their waveforms and projected images, is shown in Fig. 3. Data are acquired with our electronics system in 1 bar argon-(2.5%)isobutane gas mixtures. In the DAQ configuration, the trigger delay is set to $40\ \mu\text{s}$ to ensure that the waveforms are fully recorded within the time window and the sampling points before $11.2\ \mu\text{s}$ are used to determine the waveform baseline for charge calculation. The projected images show small-sized electron clusters generated by low-energy source events with average triggered strips of six at 1 bar. The colors in the image represent the waveform amplitude of the

event, i.e., the collected charge. Data unpacking and analysis are performed in the REST (Rare Event Searches Toolkit for Physics) [30] framework, which is a ROOT-based solution for event-oriented data analysis and Monte Carlo simulation specifically designed for gaseous TPCs.

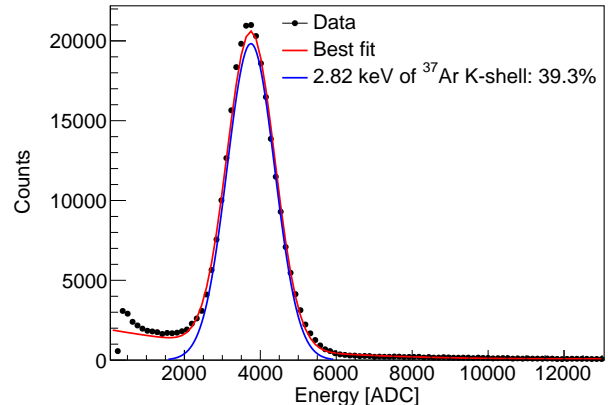


Fig. 4. (Color online) A typical energy spectrum of the ^{37}Ar K-shell decay events in 1 bar argon-(2.5%)isobutane gas mixtures.

The energy (ADC unit) of an event is determined by summing the collected charges on strips, and more specifically, by summing the waveform amplitude of over-threshold signals. Fig. 4 shows a typical energy spectrum of ^{37}Ar K-shell decay events in 1 bar argon-(2.5%)isobutane gas mixtures, where the 2.82-keV peak is fitted with a Gaussian plus a polynomial function as backgrounds. The energy resolution of the detector is expressed as the full-width-at-half-maximum (FWHM) of the Gaussian function. An energy resolution of 39.3% at 2.82 keV is obtained. The 2.82-keV peak is used to calculate the detector's gain, defined as the ratio of the total charges of primary ionized electrons after and before the detector amplification. The detector gain is about 6500 for the peak in Fig. 4 with an amplification field of 37 kV/cm and a reduced drift field of 230 V/cm/bar. Based on the acquired ^{37}Ar data, a wide range of amplification and reduced drift fields has been scanned to study the TPC performance, including electron transmission, gain, energy resolution, gain uniformity, drift field evolution, and so on.

IV. RESULTS AND DISCUSSION

A. Electron transmission, gain and energy resolution

Electron transmission is the probability of ionized electrons passing through the Micromegas mesh holes from the drift volume to the avalanche gap. It is mainly affected by two mechanisms: electron attachment and recombination in the drift volume and the transparency of the Micromegas mesh for electrons. We can calculate the gain and energy resolution with the obtained energy spectrum of ^{37}Ar K-shell decay events as mentioned in section III. The electron transmission

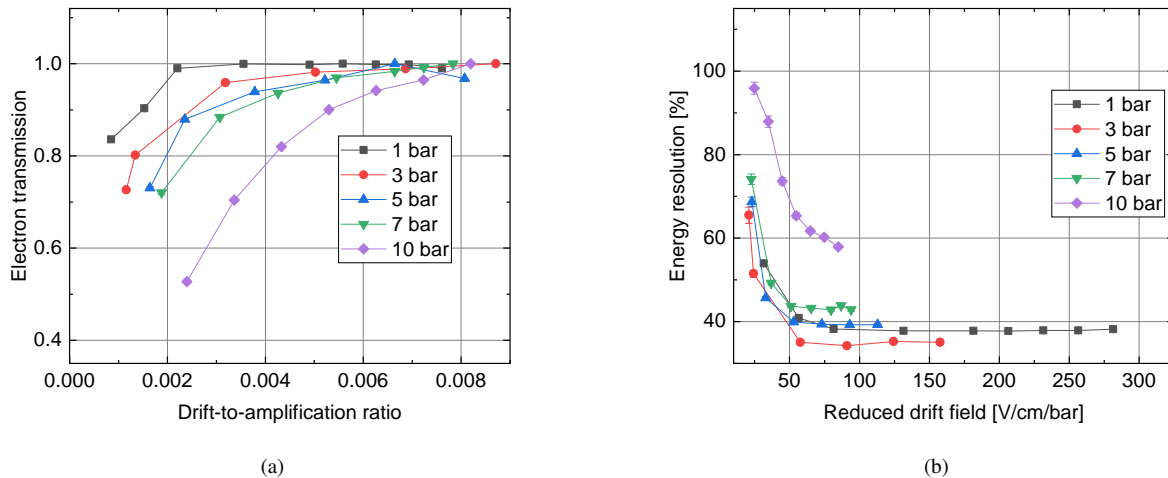


Fig. 5. (Color online) (a) Dependence of the electron transmission with the drift-to-amplification field ratio. (b) Dependence of the energy resolution with the reduced drift field.

is calculated with the gain normalized to the maximum value of each series. The drift voltage is varied at a fixed amplification voltage to obtain the dependence of the electron transmission with the drift-to-amplification field ratio from 1 bar to 10 bar argon-(2.5%)isobutane gas mixtures, as shown in Fig. 5(a). At low drift fields, the electron transmission is reduced by electron attachment and recombination of ionized electrons generated in the drift volume. At high drift fields, the plateau of electron transmission appears, indicating that the electron collection efficiency of the mesh is the highest and the attachment and recombination contributions are negligible. Accordingly, the dependence of the energy resolution with the reduced drift field (Fig. 5(b)) shows its best value at the plateau for which the electron transmission is optimal. However, it is more difficult to reach the plateau of electron transmission under high pressure, and a stronger reduced drift field is required. Especially at a pressure of 10 bar, the energy resolution deteriorates significantly compared to low-pressure measurements.

The amplification voltage is varied to study the gain of the detector with the optimal drift voltages. The gain curves in Fig. 6(a) show a linear behavior with the amplification field on the log-log plot and achieve maximum attainable gains of up to thousands at each pressure. It demonstrates the excellent performance and adaptability of the detector under different pressures. Among them, a maximum gain of 31900 is obtained with an amplification field of 38.5 kV/cm in 1 bar argon-(2.5%)isobutane gas mixtures. The maximum attainable gain reaches its best at atmospheric pressure. However, due to the Micromegas sparking, achieving a higher maximum attainable gain at very low (0.3 bar) and very high (10 bar) pressures is difficult. The energy resolution evolving with the amplification field, more specifically with the gain, is shown in Fig. 6(b). The figure shows its dependence on the absolute gain for all pressures, and the statistical error is derived from the errors in the fitting parameters of energy spec-

tra. The resolution degrades at low gains where the signal is comparable to the electronic noise. At high gains, the increase in avalanche fluctuations also leads to a degradation of the resolution [31]. The energy resolution shows its best value at a gain of about 5000 under different pressures. Specifically, an optimal energy resolution of 33.4% occurs at a working pressure of 3 bar with a gain of 5100.

B. Gain uniformity

The gain uniformity is a crucial property of the detector as it directly affects the detector's intrinsic energy resolution. It is mainly influenced by the inhomogeneity of the avalanche gap of Micromegas modules. Thanks to the uniformly distributed ^{37}Ar source and its low-energy electron clusters, the gain of the entire sensitive area of the detector can be calibrated quickly and effectively. The hit position of events is calculated with the amplitude-weighted center-of-charges method by combining the trigger position and detected charges of strip signals. The hit position in the XY readout plane indicates the central projection position of the electron cluster of events. The sensitive area is divided into 64×64 regions in the XY readout plane, and the energy spectrum in each region is reconstructed and fitted following the same procedure as shown in Fig. 4. Thus, the gain map and the energy resolution map of Micromegas can be obtained with the energy spectrum of ^{37}Ar in each region.

Fig. 7 shows a typical distribution of the mean value (peak position) and standard deviation (energy resolution) of the fit function of energy spectra in each region with an amplification field of 37 kV/cm in 1 bar argon-(2.5%)isobutane gas mixtures. The gain non-uniformity is 13.0% in this example, defined as the root mean square (RMS) of the peak distribution divided by their mean value. In the central Y and detector boundary regions, the peak position is below 2000 ADC, and

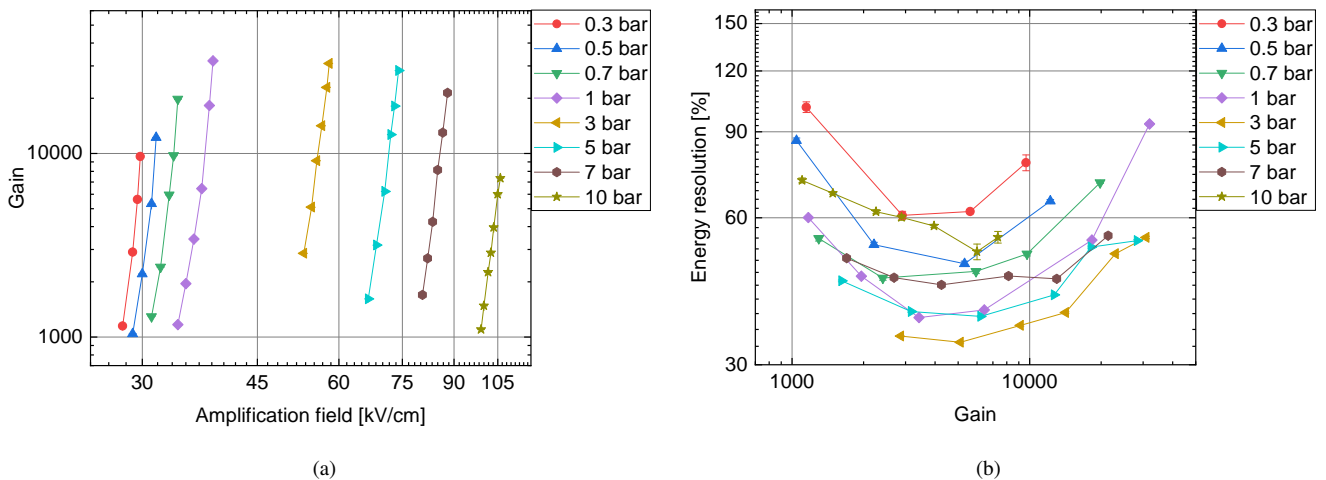


Fig. 6. (Color online) (a) Dependence of the gain with the amplification field. (b) Dependence of the energy resolution with the gain.

the energy resolution is above 80.0%. However, the average peak position in other regions is about 3600, and the average energy resolution is about 40.4%. The low peak position of the central channel in the Y direction is due to a broken electronics channel. The Micromegas border is less effective in charge collection due to the electric field distortion, resulting in an extreme degradation of the peak position and energy resolution in these regions. Moreover, for electron clusters of source events with average triggered strips of about six, falling at the edge of Micromegas also leads to incomplete charge collection of events. Thus, the dead electronics channels and low-count channels in the Micromegas border are excluded from the non-uniformity calculation. The obtained gain map, i.e. the peak position map, intuitively presents the gap uniformity of Micromegas and can be utilized to assess the detector's performance. According to [24], the surface smoothness of the readout PCB anode can affect the gap uniformity of Micromegas. Significant efforts, such as polishing and leveling the copper substrate and the PCB anode, have been made to enhance the gain uniformity and improve the stability of the detector under high pressure.

The gain map can also be applied to the charge reconstruction of the source events for uniformity correction. Gain differences between different regions lead to differences in the charge collection of source events, and uniformity correction can reduce these differences and improve the energy resolution of the detector. Fig. 8 illustrates an example of the energy spectrum without and with uniformity correction at 7 bar. After uniformity correction, the energy resolution is improved from 44.9% to 35.4%. The amplification field is varied at each pressure in the measurements. Because the relative gain of each region can not be kept constant under different amplification fields and gas mixtures, the gain map should be calibrated specifically for each pressure and amplification field. The energy resolution without and with uniformity correction from 1 to 7 bar is shown in Fig. 9. The efficiency of unifor-

mity correction becomes more pronounced in a higher pressure due to the increasing condensation of electron clusters of ^{37}Ar events. In general, the small-sized electron clusters deposited by particles lead to fewer triggered strips in the read-out plane, which means that more accurate gain maps can be obtained, and the gain maps used for uniformity correction are more efficient.

C. Drift field evolution

Uniformly distributed ^{37}Ar source provides an effective quantification of electric field distortion in the TPC. The distortion of the electric drift field deforms the drift path of ionized electrons in the TPC, diminishing the charge collection at the edges of readout planes [15]. To quantify the electric field distortion in the experiment, as shown in Fig. 10(a), the effective charge collection length (referred to as effective length) is defined as the strip distance from the edge where the count is less than 1/10 of the highest value to the readout center. The hit position map in the XY readout plane is obtained with the source events, Fig. 10(a) and Fig. 10(b) show the results in 1 bar argon-(2.5%)isobutane gas mixtures with drift voltages of -1 kV (a drift field of 31.5 V/cm) and -5 kV (a drift field of 231.5 V/cm), respectively. The mesh voltage is fixed at -370 V, corresponding to an amplification field of 37 kV/cm. The electric field distortion caused by the low drift field affects the collection efficiency of source events, resulting in a dead zone at the edge of Micromegas. Therefore, the effective length at a low drift field of 31.5 V/cm is significantly smaller than that at a high drift field of 231.5 V/cm, which has been confirmed by simulation as follows.

The electrostatic simulation of the electric field using the COMSOL Multiphysics software describes the realistic detector geometry, materials, and default electric configurations. The cathode is applied to voltages of -1 kV (for a drift

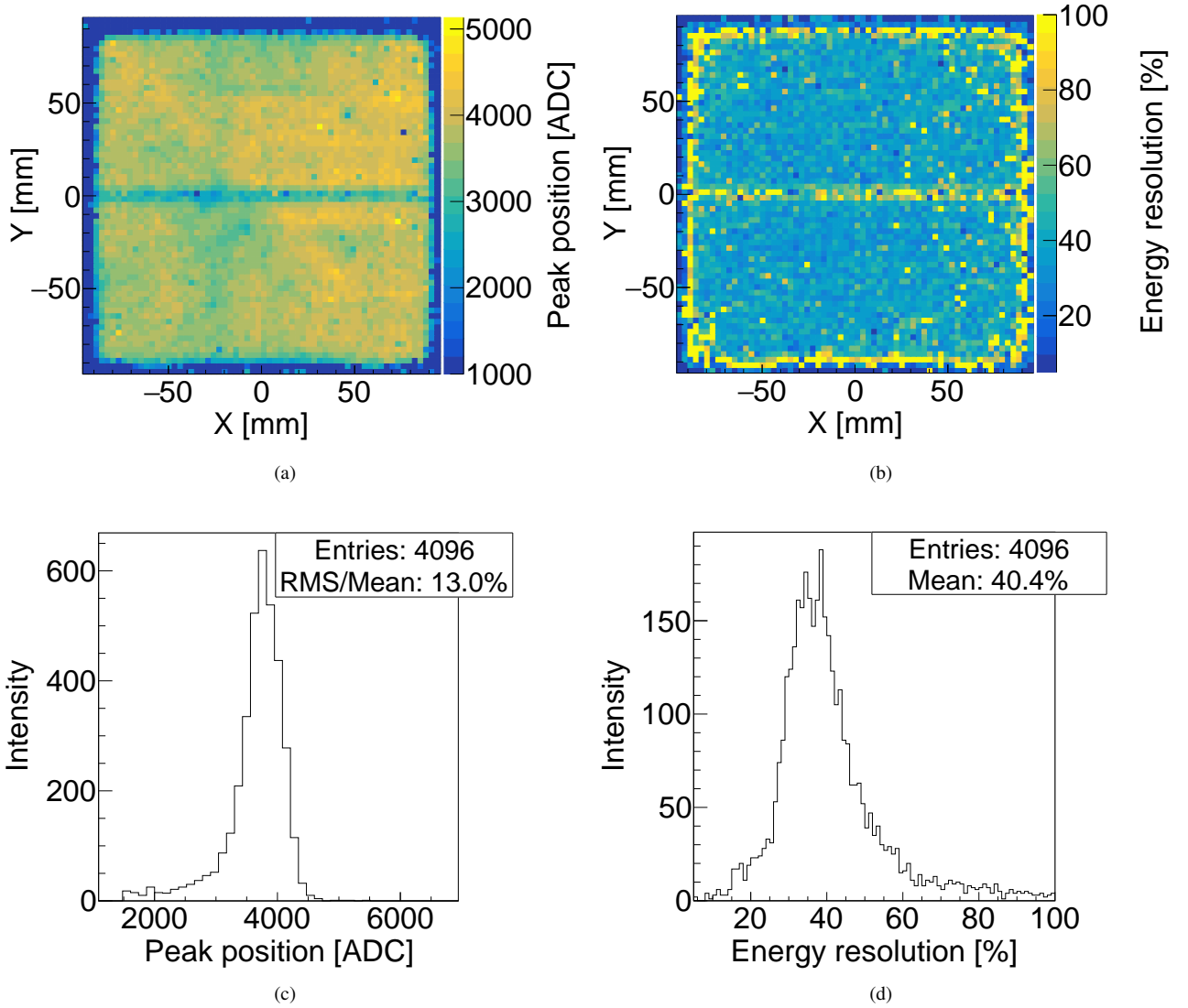


Fig. 7. (Color online) Typical two-dimensional map of the peak position (a) with the corresponding one-dimensional distribution over the 64×64 regions (c). Typical two-dimensional map of the energy resolution at 2.82 keV (b) with the corresponding one-dimensional distribution over the 64×64 regions (d).

field of 31.5 V/cm) or -5 kV (for a drift field of 231.5 V/cm), and the voltage of the copper ring closest to the readout plane is set to 0 V. The Micromegas mesh is set to a constant voltage of -370 V, and the adjacent aluminum backplate on the upper side is grounded. The vertical electric field cross-sections (i.e. the XZ plane) of the detector at electric fields of 31.5 V/cm and 231.5 V/cm are shown in Fig. 10(c) and Fig. 10(d), respectively. At a low drift field of 31.5 V/cm, the electric field distortion is pronounced at the edge of Micromegas, and the electric field lines bend at the edge. The effective length in the simulation is defined as the distance from the inflection point where the electric field lines bend at the Micromegas edge to the readout center in the X(Y) direction. The edge portion without electric field lines passing through corresponds to the dead zone of the detector. In the case of a drift field of 231.5 V/cm, the electric field distortion is negligible at the

Micromegas edges, and thus the entire readout plane is effective for event collection.

Further quantitative result of the distortion effect is illustrated in Fig. 11. We plotted the evolution of effective length with the drift field using experimental data and simulations. The results of the simulation are highly consistent with the experimental data. A 3 mm uncertainty is considered in the experiment since the pitch size of Micromegas strips is 3 mm, while the COMSOL simulation takes a millimeter level (1 mm) uncertainty due to the computational accuracy of the solver. The effective length is positively correlated with the drift field strength. Below an electric field of 56.5 V/cm, the effective length drops sharply with the decrease of the drift field. At a low electric field of 31.5 V/cm, source events can be collected in the region about 6.3 cm away from the readout center, and the peripheral region becomes a dead zone due

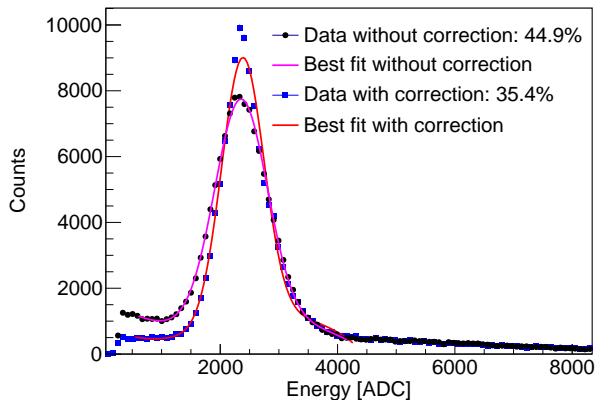


Fig. 8. (Color online) An example of the energy spectrum without and with uniformity correction at 7 bar.

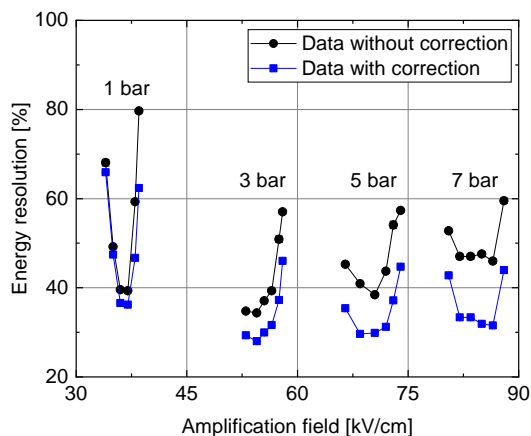


Fig. 9. (Color online) The energy resolution without and with uniformity correction from 1 to 7 bar.

to the electric field distortion. The effective length at a high electric field of 231.5 V/cm is about 9.6 cm, covering almost the entire sensitive area of the detector.

V. CONCLUSIONS

In summary, an internal calibration with ^{37}Ar is carried out to calibrate the gaseous TPC. The ^{37}Ar source is injected directly into the TPC and distributed uniformly within the active volume. The fast-decay, low-energy-deposition, and uniform-distribution features of ^{37}Ar enable us to efficiently investigate the detector performance, including electron transmission, gain, energy resolution, gain uniformity, and drift field evolution. The electron transmission is first scanned at pressures from 1 to 10 bar, and the plateau is selected to ensure the most optimized electron transparency in the experiment. The maximum attainable gain reaches up to thousands at each pressure. The limiting factor for a higher gain value is the micro-discharges between the mesh and the anode, especially at a low pressure of 0.3 bar and a high pressure of 10 bar. An optimal energy resolution is 33.4% FWHM at 2.82 keV in 3 bar argon-(2.5%)isobutane gas mixture with a gain of 5100. The gain uniformity is also calibrated with ^{37}Ar events, and a non-uniformity of 13.0% (RMS/Mean) is obtained with an amplification field of 37 kV/cm at 1 bar. The obtained gain map is used to assess the inhomogeneity of the avalanche gap of Micromegas modules. The detected charges of source events are corrected using the gain uniformity map to obtain an improved energy resolution. Due to the fact that the electron clusters of ^{37}Ar events are more concentrated under high pressure, uniformity correction is more efficient, and the energy resolution is considerably improved under high pressure. Particularly at 7 bar, the energy resolution is enhanced from 44.9% to 35.4% with the help of uniformity correction. Because of the severe electric field distortion caused by the low drift field, the effective length under the low drift field is significantly smaller than that under the high drift field. Our tests also observe the effective length of the detector evolving with the drift field, which is verified by the electric field simulation using COMSOL.

The ^{37}Ar internal calibration method has unique advantages over traditionally used ^{55}Fe source. The gaseous sources enable us to inject or remove them easily from the detector, which greatly simplifies the calibration procedure and reduces the turn-around time for physics experiments involving gaseous TPCs. The internal source also makes *in situ* calibration at low and high pressure possible. Detector performance calibrated at the same operating conditions as physics runs reduces systematic uncertainties in data analysis. For detectors that are equipped with large-area readout modules such as Micromegas, ^{37}Ar calibration emerges as an excellent and preferred choice for efficiently calibrating the entire detector readout plane. In addition, we are currently developing particle trajectory recognition algorithms with the ^{37}Ar source, which can be used for the calibration of dark matter directional detection detectors.

[1] Jay N. Marx and David R. Nygren. The Time Projection Chamber. *Phys. Today*, 31N10:46–53, 1978.

[2] Ishaan Ahuja. Looking for collective origin of strangeness enhancement in small collision systems with ALICE at the LHC.

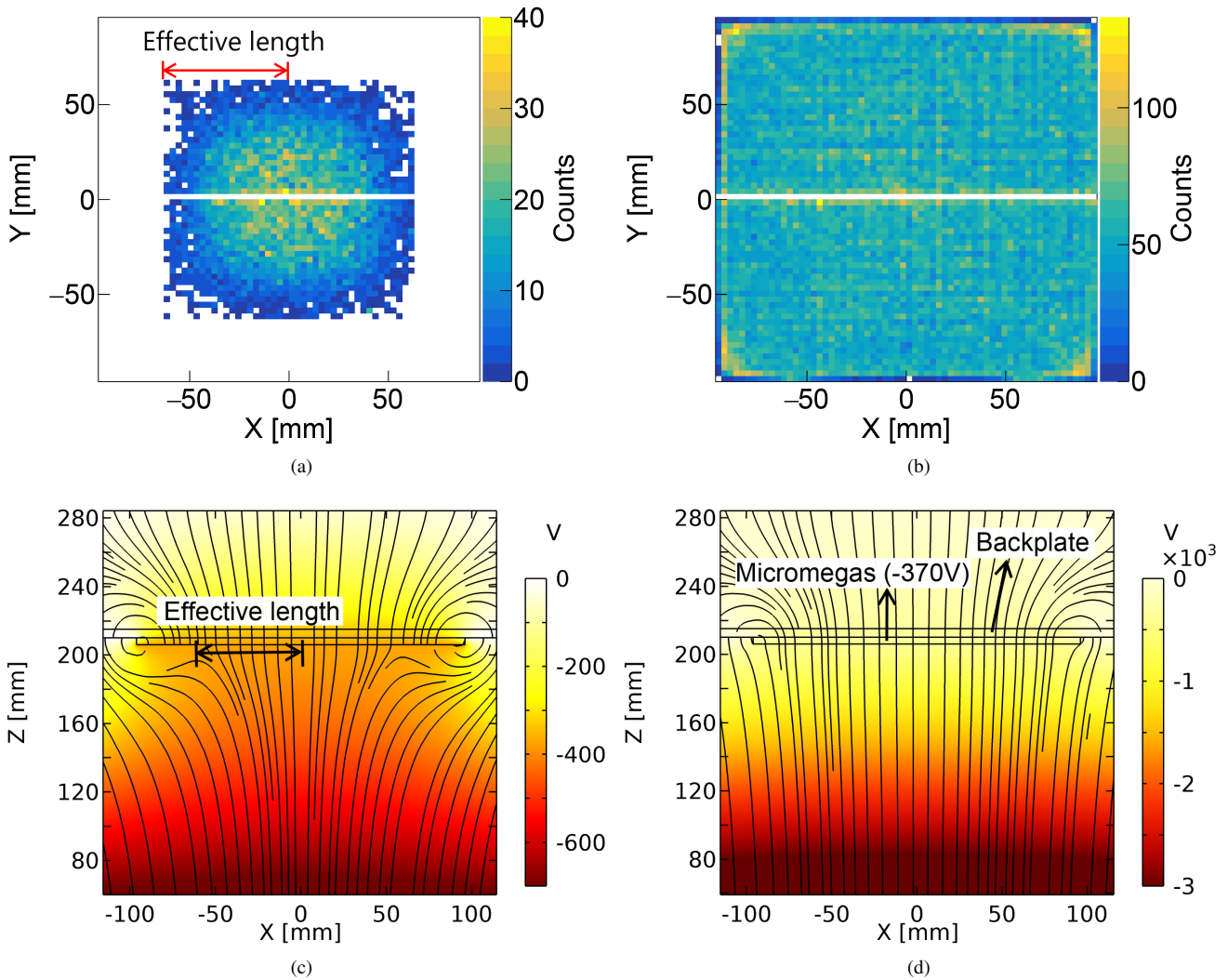


Fig. 10. (a) A hit position map of source events in the XY readout plane at a drift field of 31.5 V/cm. (b) A hit position map of source events in the XY readout plane at a drift field of 231.5 V/cm. (c) Vertical electric field cross-section of the detector at a drift field of 31.5 V/cm simulated with COMSOL. (d) Vertical electric field cross-section of the detector at a drift field of 231.5 V/cm simulated with COMSOL.

- PoS*, HardProbes2023:122, 2024.
- [3] K. H. Ackermann et al. STAR detector overview. *Nucl. Instrum. Meth. A*, 499:624–632, 2003.
- [4] Miryam Martínez-Vara. NEXT, a neutrinoless double beta decay experiment. *PoS*, EPS-HEP2023:169, 2024.
- [5] Shaobo Wang. The TPC detector of PandaX-III Neutrinoless Double Beta Decay experiment. *JINST*, 15(03):C03052, 2020.
- [6] Wenming Zhang, Heng Lin, Yuanchun Liu, Ke Han, Kaixiang Ni, Shaobo Wang, and Wenchang Zhai. Status and prospects of the PandaX-III experiment. *JINST*, 18(12):C12001, 2023.
- [7] R. Bouet et al. R2D2 TPC: first Xenon results. *JINST*, 18(10):T10001, 2023.
- [8] Xi-Guang Cao et al. $N\nu$ DEX-100 conceptual design report. *Nucl. Sci. Tech.*, 35(1):3, 2024.
- [9] Juan F. Castel et al. Searching for WIMPs with TREX-DM: achievements and challenges. 12 2023.
- [10] G. Gerbier et al. NEWS : a new spherical gas detector for very low mass WIMP detection. 1 2014.
- [11] M. Laubenstein, B. Lehnert, and S. S. Nagorny. First limits on double beta decays in ^{232}Th . *Eur. Phys. J. C*, 80(8):759, 2020.
- [12] C. W. Fink et al. Performance of a large area photon detector for rare event search applications. *Appl. Phys. Lett.*, 118(2):022601, 2021.
- [13] M. Kobayashi et al. Cosmic ray tests of a GEM-based TPC prototype operated in Ar-CF₄-isobutane gas mixtures. *Nucl. Instrum. Meth. A*, 641:37–47, 2011. [Erratum: *Nucl. Instrum. Meth. A* 697, 122 (2013)].
- [14] B. Aimard et al. Performance study of a $3\times 1\times 1$ m³ dual phase liquid Argon Time Projection Chamber exposed to cosmic rays. *JINST*, 16(08):P08063, 2021.
- [15] Wenming Zhang et al. Calibration of a Micromegas-based gaseous time projection chamber using cosmic ray muons. *JINST*, 18(07):P07038, 2023.
- [16] S. Sangiorgio et al. First demonstration of a sub-keV electron recoil energy threshold in a liquid argon ionization chamber. *Nucl. Instrum. Meth. A*, 728:69–72, 2013.

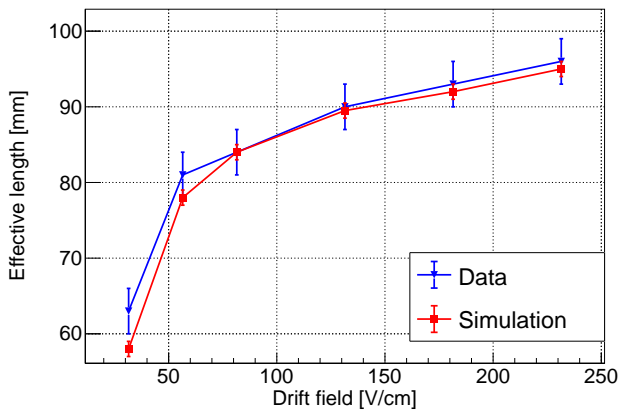


Fig. 11. (Color online) Dependence of the effective length with the drift field.

- [17] D. Yu. Akimov et al. Experimental study of ionization yield of liquid xenon for electron recoils in the energy range 2.8 - 80 keV. *JINST*, 9(11):P11014, 2014.
- [18] E. M. Boulton et al. Calibration of a two-phase xenon time projection chamber with a ^{37}Ar source. *JINST*, 12(08):P08004, 2017.
- [19] L. Baudis, Y. Biondi, M. Galloway, F. Girard, S. Hochrein, S. Reichard, P. Sanchez-Lucas, K. Thieme, and J. Wulf. The first dual-phase xenon TPC equipped with silicon photomultipliers and characterisation with ^{37}Ar . *Eur. Phys. J. C*, 80(5):477, 2020.
- [20] E. Aprile et al. Low-energy calibration of XENON1T with an internal ^{37}Ar source. *Eur. Phys. J. C*, 83(6):542, 2023.
- [21] Ö Şahin, İ Tapan, E. N. Özmütlu, and R. Veenhof. Penning transfer in argon-based gas mixtures. *JINST*, 5(05):P05002, 2010.
- [22] Y. Giomataris, P. Rebourgeard, J. P. Robert, and Georges Charpak. MICROMEGAS: A High granularity position sensitive gaseous detector for high particle flux environments. *Nucl. Instrum. Meth. A*, 376:29–35, 1996.
- [23] COMSOL Multiphysics V. 6.1. Comsol AB, Stockholm, Sweden. <https://www.comsol.com>.
- [24] Sicheng Wen, Zhiyong Zhang, Yunzhi Peng, Ke Han, Shaobo Wang, Changqing Feng, Shubin Liu, Jianbei Liu, Ming Shao, and Yi Zhou. Design and fabrication of low background, high energy resolution thermal bonding Micromegas detectors for the PandaX-III experiment. *Nucl. Instrum. Meth. A*, 1062:169206, 2024.
- [25] Jianxin Feng, Zhiyong Zhang, Jianbei Liu, Binbin Qi, Anqi Wang, Ming Shao, and Yi Zhou. A thermal bonding method for manufacturing Micromegas detectors. *Nucl. Instrum. Meth. A*, 989:164958, 2021.
- [26] Jianxin Feng, Zhiyong Zhang, Jianbei Liu, Ming Shao, and Yi Zhou. A novel resistive anode using a germanium film for Micromegas detectors. *Nucl. Instrum. Meth. A*, 1031:166595, 2022.
- [27] J. Giovinazzo et al. GET electronics samples data analysis. *Nucl. Instrum. Meth. A*, 840:15–27, 2016.
- [28] S. Anvar et al. Aget, the get front-end ASIC, for the readout of the time projection chambers used in nuclear physics experiments. *2011 IEEE Nuclear Science Symposium Conference Record*, pages 745–749, 2011.
- [29] SAES Getters Group. <https://www.saesgetters.com/>.
- [30] Konrad Altenmüller et al. REST-for-Physics, a ROOT-based framework for event oriented data analysis and combined Monte Carlo response. *Comput. Phys. Commun.*, 273:108281, 2022.
- [31] H. Schindler, S. F. Biagi, and R. Veenhof. Calculation of gas gain fluctuations in uniform fields. *Nucl. Instrum. Meth. A*, 624(1):78–84, 2010.